Chinese Chemical Letters 34 (2023) 108099

Contents lists available at ScienceDirect

Chinese Chemical Letters

journal homepage: www.elsevier.com/locate/cclet

Novel colorimetric, photothermal and up-conversion fluorescence triple-signal sensor for rosmarinic acid detection

Yinyin Chen[a,c,1], Xiujuan Yang[a,c,1], Changfang Lu[b], Zouping Yang[b], Wei Wu[a,c,*], Xianxiang Wang[b,**]

[a] College of Agronomy, Sichuan Agricultural University, Chengdu 611130, China
[b] College of Science, Sichuan Agricultural University, Chengdu 611130, China
[c] State Key Laboratory of Crop Gene Exploration and Utilization in Southwest China, Chengdu 611130, China

ARTICLE INFO

Article history:
Received 13 June 2022
Revised 1 December 2022
Accepted 22 December 2022
Available online 26 December 2022

Keywords:
Multi-modal sensing
Up-conversion fluorescence
Colorimetric
Photothermal
Rosmarinic acid

ABSTRACT

Rosmarinic acid (RA) is promising as a natural and nontoxic food additive. However, many analysis methods for RA generally depend on large instruments and single signals for quantitative detection. A new up-conversion fluorescence, colorimetric and photothermal multi-modal sensing strategy is developed for the quantification of RA. β-cyclodextrin (CD) modified citric acid (Cit) wrapped $NaYF_4$:Yb/Er-Cit-CD (Y:Yb/Er-Cit-CD) up-conversion nanocomposite has been synthesized, which emits green fluorescence at 550 nm under 980 nm near-infrared (NIR) excitation. In the presence of oxidized 3,3′,5,5′-tetramethylbenzidine (oxTMB), the green fluorescence is significantly quenched attributed to the fluorescence inner filter effect (IFE) between oxTMB and Y:Yb/Er-Cit-CD. When RA is intervened, blue oxTMB is reduced to colorless 3,3′,5,5′-tetramethylbenzidine (TMB) inducing the recovery of up-conversion fluorescence. At the same time, colorimetric and photothermal signals readout can be easily achieved thanks to the color indication and photothermal effect of the oxTMB. The constructed Y:Yb/Er-Cit-CD/oxTMB sensor displays high sensitivity, visibility and simplicity for RA, and the limits of detection (LOD) for fluorescence, colorimetric and photothermal were 0.004 μmol/L, 0.036 μmol/L and 0.043 μmol/L, respectively. This sensing system is successfully performed for the detection of RA in food samples.

Rosmarinic acid (RA) is a natural phenolic acid containing several phenolic hydroxyl groups [1]. It is widely found in Lamiaceae plants, such as *Salvia miltiorrhiza Bunge*, *Rosmarinus officinalis*, and *Perilla frutescens* [2]. RA has been found to have antioxidant, antibacterial and anti-inflammatory activities [3–5], which is a valuable candidate product for inclusion in functional foods and pharmaceutical plant products. In addition, RA is expected to be effective in preventing Alzheimer's disease due to its inhibition of amyloid-β aggregation [6]. These various application prospects contribute to the great interest in RA component. In order to facilitate the subsequent applications, a series of techniques for the determination of RA have been reported, including high performance liquid chromatography (HPLC) [7], liquid chromatography-mass spectrometry (LC-MS) [8], ultraviolet spectrophotometry [9] and capillary electrophoresis (CE) [10]. Among the mentioned methods, the HPLC method is frequently used for the quantification of RA because of its excellent separation efficiency, accuracy and sensitivity. Unfortunately, it still has some inherent limitations, such as cumbersome sample pre-processing, reliance on large instruments and technical requirements for instrument operators. The development of analytical methods with simple operation, free of complex instrumentation, good selectivity and high sensitivity is a hot spot in current research.

Sensor detection is a method of qualitative or quantitative analysis of the target by converting the recognized signal into other various signals and outputting them. It has many excellent features, including miniature equipment, high sensitivity, good selectivity, simple operation and rapid response. In recent years, this method has shown great potential in the fields of environmental monitoring, food analysis, and biomedicine [11–14]. As we all know, fluorescence sensor is regarded as one of the most sensitive analysis tools, and has a considerable research foundation [15–17]. The excitation light source of traditional down-conversion

* Corresponding author at: College of Agronomy, Sichuan Agricultural University, Chengdu 611130, China.
** Corresponding author.
E-mail addresses: ewuwei@sicau.edu.cn (W. Wu), xianxiangwang@hotmail.com (X. Wang).
[1] These authors contributed equally to this work.

https://doi.org/10.1016/j.cclet.2022.108099
1001-8417/

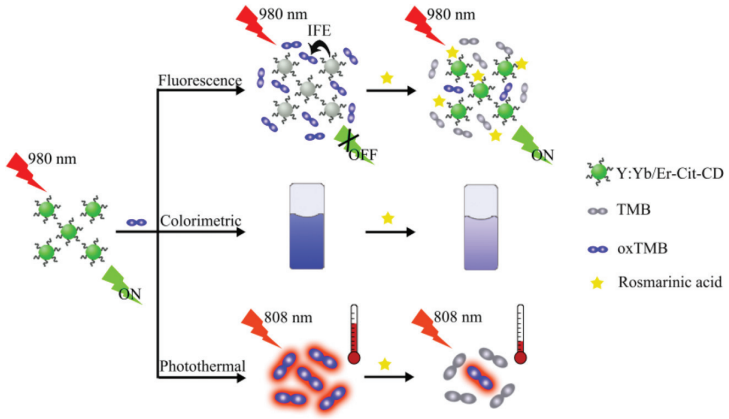

Scheme 1. Schematic diagram of the Y:Yb/Er-Cit-CD/oxTMB sensor for RA detection.

fluorescence is ultraviolet light, having the drawbacks of background interference, short lifetime and easy photo drift, thus its development is hindered greatly. As a meaningful alternative, up-conversion nanoparticles (UCNPs) have attracted more and more attention and have been widely used in the fluorescence sensor [18–20]. UCNPs usually transform low-energy light into high-energy light. The biological sample absorbs less of this low-energy infrared light, which can effectively avoid the fluorescence interference of the biological sample itself. Therefore, this material has the advantages of non-autofluorescence, non-photobleaching and low damage to biological tissues, which is unique in the field of biosensing and bioimaging [21–23]. Regrettably, the readout of the fluorescence signal is also directly dependent on sophisticated instrumentation, thus unsatisfied with the demands of portable detection. Furthermore, analysis by single signal changes may be susceptible to incidental factors such as instrument efficiency, operating and measurement conditions, and unstable biological environments. To achieve portable and sensitive probes, several research groups have proposed the analysis strategy of constructing a multi-mode sensing platform [24–26]. Colorimetric sensors and photothermal sensors provide important avenues for this strategy. The colorimetric sensor is based on the color shade of colored substance to achieve the determination of component content [27,28]. Since the color change can be observed by the naked eye, it has the advantage of direct readout and simplicity. Colorless 3,3′,5,5′-tetramethylbenzidine (TMB) is a relatively safe and stable chromogen reagent, which can be oxidized to blue oxidized 3,3′,5,5′-tetramethylbenzidine (oxTMB). Studies have confirmed that TMB has been widely used in colorimetric detection [29,30]. Photothermal sensors can be realized by using the photothermal effect of substances [31]. After the substance is irradiated with near-infrared (NIR) light, the temperature will change. The content of the target component can be determined by measuring the temperature change of the substance solution. Photothermal readout only requires a portable thermometer and a NIR laser without complex control equipment, which greatly reduces development costs and the complexity of the analysis process. Therefore, photothermal detection through thermometer readout plays an important role in point-of-care detection [27]. oxTMB has been widely demonstrated to be a novel photothermal probe. It is simple and easy to obtain without any tedious preparation process, and has been applied to some photothermal sensors [31,32]. Therefore, the multi-signal sensing platform that integrates fluorescent signal with colorimetric signal and photothermal signal can combine the advantages of different single-signal technologies to meet the requirements of sensitive, visible, and portable detection. Moreover, the methods can be validated against each other to further provide reliable and accurate quantitative results.

In this work, a new up-conversion fluorescence, colorimetric and photothermal multi-modal analysis method for the quantification of RA has been developed. The principle of the sensing system is shown in Scheme 1. β-Cyclodextrin (CD) modified citric acid (Cit) coated $NaYF_4$:Yb/Er-Cit-CD (Y:Yb/Er-Cit-CD) up-conversion nanocomposite has been synthesized and has good dispersibility in water. Under 980 nm NIR irradiation, Y:Yb/Er-Cit-CD emits green fluorescence with a spectral peak of about 550 nm. The emission spectrum partially overlapped with the absorption spectrum of oxTMB. Therefore, the green fluorescence of Y:Yb/Er-Cit-CD can be effectively quenched by the oxTMB because of the fluorescence inner filter effect (IFE). When RA is introduced, the blue oxTMB is reduced to colorless TMB. Since the absence of IFE between TMB and Y:Yb/Er-Cit-CD, up-conversion fluorescence is recovered and sensitive fluorescence detection is achieved. At the same time, the decrease in absorbance of the system can be easily observed with naked eye due to the color indication of oxTMB. In addition, oxTMB also has the photothermal effect, converting light to heat under 808 nm laser irradiation and reading out the photothermal signal by measuring the change in system temperature with a thermometer. Based on this principle, a new sensitive, visible and convenient method for the detection of RA is provided, and applied successfully to the detection of RA in food samples.

Y:Yb/Er has been synthesized by the high-temperature solvothermal method. The produced Y:Yb/Er-OA is hydrophobic because its surface has been covered with OA. When Y:Yb/Er-OA has been converted into hydrophilic, the Cit-CD coating is encapsulated with the help of EDC/NHS to improve the dispersibility of nanoparticles in water. Fig. 1 shows the TEM, HRTEM, EDX and XRD images of Y:Yb/Er. As displayed in Fig. 1a, the obtained Y:Yb/Er nanoparticles are monodisperse in chloroform and the shape is close to hexagonal with a size of about 23 nm. From Fig. 1b, the lattice stripes of Y:Yb/Er can be clearly seen with a stripe spacing of 0.23 nm, corresponding to the (111) plane of hexagonal β-Y:Yb/Er. The EDX spectrum of Y:Yb/Er is exhibited in Fig. 1c, and the characteristic peaks of Na, Y, F, Yb, C and O elements are clearly observed (due to the low amount of Er element, there is no eyeable peak in the spectrum). Fig. 1d displays the XRD pattern of Y:Yb/Er, demonstrating that the nanoparticles are primarily consisted of hexagonal phase. The above results indicate the successful synthesis of Y:Yb/Er. Then, the prepared Cit-CD has been characterized by spectrophotometer and Fourier transform infrared spectrometer. The UV-vis absorption spectra of Cit, CD, Cit + CD and Cit-CD are shown in Fig. 2a. Black curve represents Cit, which has a pronounced absorption at 234 nm. Red curve represents CD, with a weak absorption peak at 215 nm. Blue curve represents Cit + CD, whose absorption spectrum is similar to Cit and is a simple superposition of Cit and CD. Green curve represents Cit-CD,

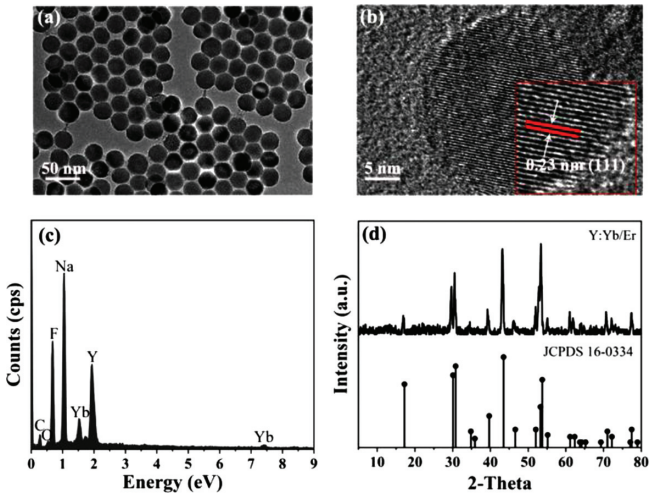

Fig. 1. (a) TEM, (b) HRTEM, (c) EDX and (d) XRD patterns of Y:Yb/Er.

which has an absorption peak at 200 nm and it is clearly distinct from the spectra of the three substances as-mentioned. The FT-IR spectra of Cit, CD, and Cit-CD have been analyzed as shown in Fig. 2b. Blue curve represents Cit, and the characteristic band at 1717 cm^{-1} originates from the stretching vibration of the C=O bond. Black curve represents CD, and the absorption bands at 3390 cm^{-1} and 1027 cm^{-1} are attributed to the stretching vibration of the O-H bond and the stretching vibration of the C-O bond, respectively. Red curve represents Cit-CD, and the absorption bands at 3408 cm^{-1} and 1726 cm^{-1} result from the stretching vibration of the O-H bond and the stretching vibration of the C=O bond, respectively. These data have indicated that Cit and CD are well connected to obtain Cit-CD. And the combined yield of Cit and CD has been calculated to be about 92.25%.

Subsequently, the UV-vis absorption spectrum, FT-IR spectrum, EDX pattern, TEM image and major element mapping of Y:Yb/Er-Cit-CD have been measured. Fig. 2c illustrates the UV-vis absorption spectra of Cit-CD, Y:Yb/Er, Y:Yb/Er + Cit-CD and Y:Yb/Er-Cit-CD. The absorption spectrum of Y:Yb/Er-Cit-CD (green curve) is different from the Cit-CD (black curve), Y:Yb/Er (red curve) and the simple mixture of these two substances (blue curve). Then, Fig. 2d displayed the FT-IR spectra of Y:Yb/Er, Cit-CD and Y:Yb/Er-Cit-CD. Compared with the spectrum of Y:Yb/Er (black curve), the 1715 cm^{-1} characteristic peak of Y:Yb/Er-Cit-CD (red curve) has represented the stretching vibration of the C=O bonds of Cit in Cit-CD. The 1108 cm^{-1} characteristic band can belong to the stretching vibration of the C-O single bond in Cit-CD. The EDX pattern of Y:Yb/Er-Cit-CD in Fig. 2e illustrates that the peak heights of Na and C elements are apparently different from the Y:Yb/Er. As shown in Fig. 2f, Y:Yb/Er-Cit-CD is uniformly wrapped with the Cit-CD shell layer, which is about 25 nm in size and slightly larger than Y:Yb/Er. Besides, Y:Yb/Er-Cit-CD has good dispersibility in aqueous solution. The STEM image and main elemental mapping images of Y:Yb/Er-Cit-CD have been tested in Fig. 2g. O, F, Y, Yb and Er elements are homogeneously distributed in the Y:Yb/Er-Cit-CD nanocomposite, with the largest amount of O elements, further demonstrating that Cit-CD is uniformly encapsulated on the surface of Y:Yb/Er. Besides, the synthesized MnO_2 has been identified by TEM image and XRD pattern. As seen in Fig. S1a (Support information), the MnO_2 exhibits a uniform and transparent thin-layer flake structure, and its crystal structure is shown in Fig. S1b (Support information). The obtained results are consistent with the reference method [33].

According to the principle of the IFE, when the emission spectrum of fluorophore roughly overlaps with the absorption spectrum of absorbing substance, resulting in weaker fluorescence intensity of fluorophore [34–36]. As shown in Fig. 3a, curve a represents the fluorescence emission spectrum of Y:Yb/Er-Cit-CD under 980 nm NIR radiation. The green characteristic band of Er^{3+} centered at 550 nm is derived from $^4S_{3/2} \rightarrow {}^4I_{15/2}$ transition. Curve c shows the absorption spectrum of TMB and almost no absorp-

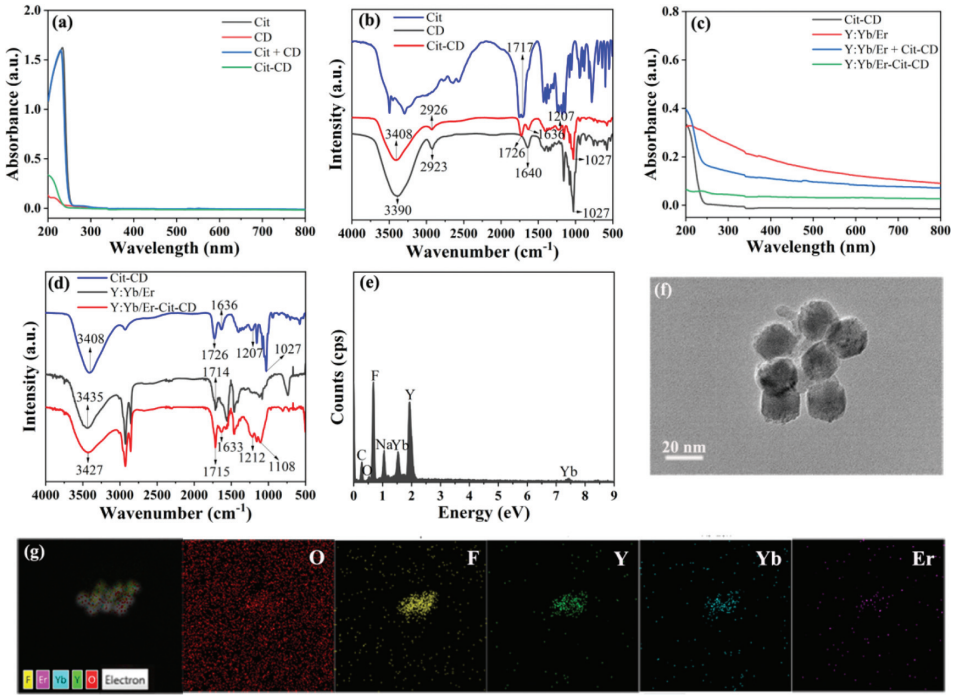

Fig. 2. (a) UV–vis absorption spectra of Cit, CD, Cit + CD and Cit-CD. (b) FT-IR spectra of Cit, CD, and Cit-CD. (c) UV–vis absorption spectra of Cit-CD, Y:Yb/Er, Y:Yb/Er + Cit-CD and Y:Yb/Er-Cit-CD. (d) FT-IR spectra of Cit-CD, Y:Yb/Er, and Y:Yb/Er-Cit-CD. (e) EDX pattern and (f) TEM image of Y:Yb/Er-Cit-CD. (g) STEM image of Y:Yb/Er-Cit-CD and corresponding elemental mapping images.

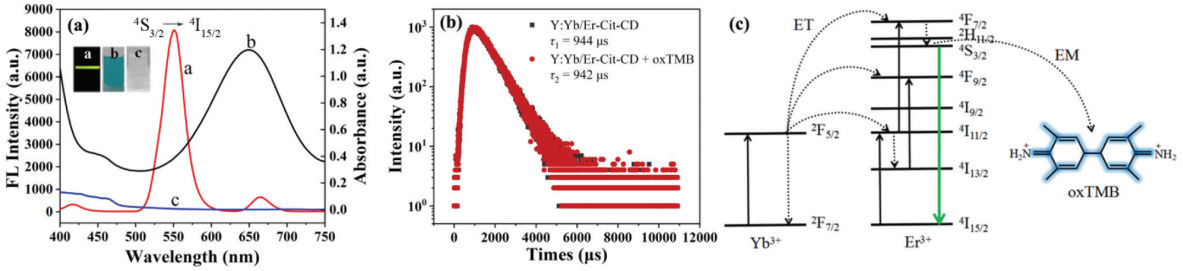

Fig. 3. (a) The fluorescence emission spectrum of Y:Yb/Er-Cit-CD and the UV–vis absorption spectrum of oxTMB and TMB. The insets are corresponding fluorescent visualizations and solution color photographs. (b) The decay dynamics for $^4S_{3/2} \rightarrow {}^4I_{15/2}$ transition of Y:Yb/Er-Cit-CD without and with of oxTMB (250 μmol/L). (c) The excitation and IFE mechanism in Y:Yb/Er-Cit-CD/oxTMB system.

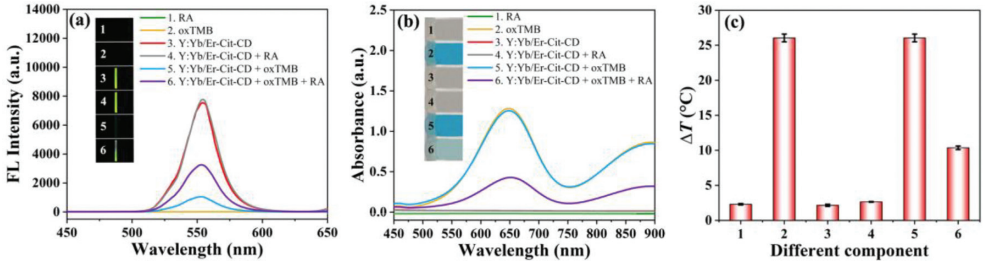

Fig. 4. The (a) fluorescence emission spectra, (b) UV–vis absorption spectra and (c) temperature changes of different components. The insets are the corresponding fluorescent visualization photograph and solution color photograph, respectively.

tion. However, when TMB is oxidized to oxTMB (curve b) with MnO_2 nanosheets, there is a UV-vis absorption peak region at 550–750 nm. One can clearly see the absorption band of oxTMB overlapping with the fluorescence emission band of Y:Yb/Er-Cit-CD, providing the conditions for fluorescence quenching. Fig. 3b shows that the absence and presence of oxTMB (0.25 mmol/L) have almost no effect on the fluorescence decay life for $^4S_{3/2} \rightarrow {}^4I_{15/2}$ transition of Y:Yb/Er-Cit-CD. This result has suggested that fluorescence resonance energy transfer (FRET) is not the reason of quenching. Then, the absorbance of oxTMB is almost unchanged in the presence of Y:Yb/Er-Cit-CD (Fig. S2 in Supporting information), which rules out static quenching induced by the formation of non-luminescent ground-state complexes between the phosphor and the quencher. Based on the above phenomena, we have speculated that the explanation for fluorescence quenching can be attributed to the IFE induced by the absorption of emitted light from Y:Yb/Er-Cit-CD by oxTMB, which is consistent with the reported literature [34,36,37]. Fig. 3c further shows the energy transfer of Y:Yb/Er-Cit-CD under 980 nm NIR radiation and the IFE mechanism of Y:Yb/Er-Cit-CD/oxTMB system. First, Yb^{3+} ions are pumped from the ground state ($^2F_{7/2}$) to the excited state ($^2F_{5/2}$) by absorbing photons. Then, energy transfers from Yb^{3+} to Er^{3+} ions through three pathways, with the $^4I_{11/2}$, $^4F_{9/2}$ and $^4F_{7/2}$ energy levels being populated. Er^{3+} ions can be excited from $^4I_{11/2}$ state to $^4F_{7/2}$ state. The $^4F_{7/2}$ level decays non-radiatively to the $^4S_{3/2}$ level, which is followed by the $^4S_{3/2} \rightarrow {}^4I_{15/2}$ transition leading to the characteristic green emission of Er^{3+} at 550 nm. When quencher oxTMB is added, the $^4S_{3/2}$ state energy emission of Er^{3+} is absorbed by oxTMB, leading to quenching of the fluorophore green fluorescence.

The feasibility of the triple-signal system for detecting RA has been assessed, and the results are displayed in Fig. 4. First, Fig. 4a shows the fluorescence emission spectra of different components. The fluorescence of Y:Yb/Er-Cit-CD (red curve) is overtly quenched in the presence of oxTMB (blue Curve). When a certain concentration of RA is mixed in Y:Yb/Er-Cit-CD/oxTMB solution, the fluorescence recovered due to the reduction of oxTMB to TMB and the absence of IFE (purple curve). The inset shows the corresponding fluorescence visualization photograph of the different component solutions under the exposure of 980 nm laser, which are consistent with the fluorescence measurements. Then, the UV-vis absorption spectra of different components is shown in Fig. 4b. The Y:Yb/Er-Cit-CD solution has no observable absorption in the region of 500–750 nm (red curve), and the solution is almost colorless and transparent. When oxTMB has been added, the Y:Yb/Er-Cit-CD/oxTMB solution has a distinct absorption peak at 650 nm (blue curve) and the solution is blue. Following the introduction of RA, the absorption of the solution at 650 nm is weakened (purple curve) and the color of the solution becomes lighter owing to the reduction of oxTMB to TMB. Afterwards, the readout of the photothermal signal has been analyzed based on the good absorption at 808 nm (Fig. 4b) and photothermal effects of oxTMB. The results of the temperature changes of different component solutions under 808 nm laser irradiation are shown in Fig. 4c. Among them, the temperature of the solution containing oxTMB has increased significantly, but no notable changes have been observed in other solutions. These phenomena demonstrate the possibility of Y:Yb/Er-Cit-CD/oxTMB sensing system to read out RA through the triple-signal of fluorescence, colorimetric and photothermal.

In order to obtain the best sensing performance for RA, the parameters of the experimental conditions have been divided into two groups to optimize, including fluorescence quenching group and fluorescence recovery group. The fluorescence quenching group of Y:Yb/Er-Cit-CD/oxTMB relates to the acidity, temperature, time of the reaction between Y:Yb/Er-Cit-CD and oxTMB, and the amount of oxTMB. Fig. S3 (Supporting information) shows the optimization results of oxTMB quenching the fluorescence of Y:Yb/Er-Cit-CD. As displayed in Fig. S3a, the acidity of the reaction has a great effect on the fluorescence intensity of the system at 550 nm. In order to achieve the best quenching effect, pH 5 has been selected as the appropriate acidity for the reaction. Then, the effect of reaction temperature on fluorescence quench-

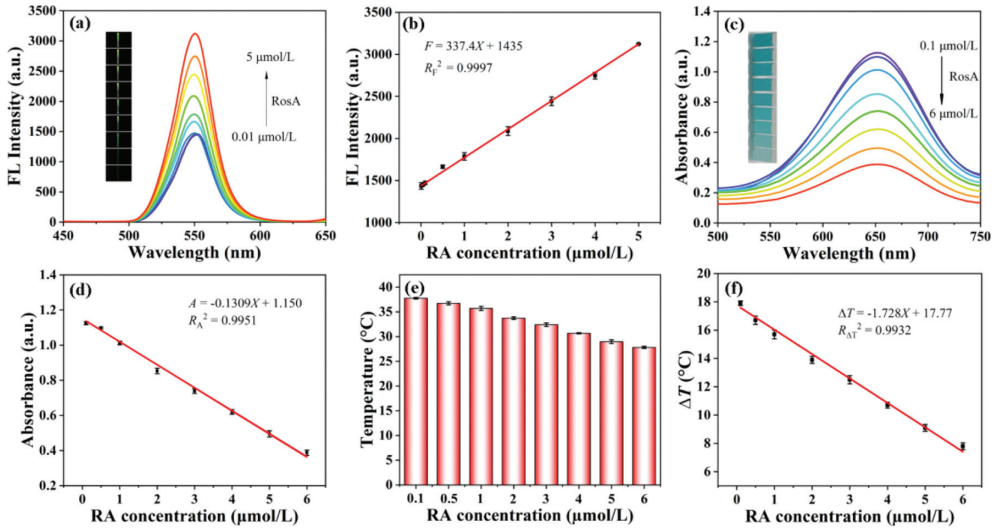

Fig. 5. (a) Fluorescence emission spectra of the sensing system in the presence of different RA concentrations. The inset is the fluorescence visualization photograph of the solution under different RA concentrations, from bottom to top are 0.01, 0.05, 0.1, 0.5, 1, 2, 3, 4 and 5 μmol/L. (b) Linear relationship between fluorescence intensity at 550 nm and the concentration of RA (0.01, 0.05, 0.1, 0.5, 1, 2, 3, 4, 5 μmol/L). (c) UV–vis absorption spectra of sensing system with different RA concentrations (0.1, 0.5, 1, 2, 3, 4, 5, 6 μmol/L). The inset is the color photograph of the system at different RA concentrations. (d) Linear relationship between absorbance at 650 nm and the concentration of RA (0.1, 0.5, 1, 2, 3, 4, 5, 6 μmol/L). (e) Temperature of sensing system with different RA concentrations (0.1, 0.5, 1, 2, 3, 4, 5, 6 μmol/L) after 808 nm laser irradiation for 5 min. (f) Linear relationship between the temperature change after 808 nm laser irradiation for 5 min and the concentration of RA (0.1, 0.5, 1, 2, 3, 4, 5, 6 μmol/L).

ing has been investigated with the temperature controlled at 15 °C to 60 °C (Fig. S3b). The lowest fluorescence intensity is obtained at the reaction temperature of 30 °C. Therefore, 30 °C has been chosen as the optimum reaction temperature. Fig. S3c represents the relationship between reaction time and fluorescence quenching for the addition of oxTMB into Y:Yb/Er-Cit-CD system. The fluorescence intensity is minimized and stabilized when the reaction time is 30 min, thus 30 min has been decided as the optimized reaction time. Next, the influence of oxTMB content on the fluorescence quenching of Y:Yb/Er-Cit-CD has been examined. The oxTMB was prepared by the oxidase (OXD) activity of MnO_2 nanosheets. As shown in Fig. S4a (Supporting information), MnO_2 nanosheets can effectively catalyze the oxidation of TMB into blue oxTMB in a concentration (Fig. S4b in Supporting information) and time (Fig. S4c in Supporting information) dependent manner. Then, the effects of pH condition (Fig. S4d in Supporting information) and reaction temperature (Fig. S4e in Supporting information) on the OXD activity of MnO_2 nanosheets showed that the optimal activity has been obtained at pH 5.0 and 40 °C. Fig. S4f (Supporting information) shows the typical Michaelis kinetics of TMB catalytic oxidation by MnO_2 nanosheets, with the Michaelis-Menten constant (K_m) is 0.3630 mmol/L and the maximal reaction velocity (V_{max}) is 6.4475 μmol L^{-1} s^{-1} (Fig. S4g in Supporting information). These results indicate that MnO_2 nanosheets exhibit excellent OXD catalytic activity. Subsequently, the quenching efficiency of TMB to Y:Yb/Er-Cit-CD has been evaluated with TMB concentrations ranging from 0.025 mmol/L to 0.5 mmol/L (Fig. S4h in Supporting information). With the increases of TMB concentration, the fluorescence quenching efficiency gradually improves, reaching a maximum and stabilizing when the concentration of TMB increases to 0.25 mmol/L. Therefore, 0.25 mmol/L has been preferred as the optimum quenching concentration. The fluorescence recovery group of Y:Yb/Er-Cit-CD/oxTMB/RA includes the acidity, temperature and time of the incubation for RA detection. As seen in Fig. S5a (Supporting information), the fluorescence intensity can recover to the maximum at pH 7. Fig. S5b (Supporting information) indicates that the fluorescence intensity is brightest when the incubated temperature is maintained at 40 °C. In Fig. S5c (Supporting information), the result has suggested that the fluorescence intensity gradually enhances with extended incubation time, and the fluorescence intensity reaches the maximum and remains steady when the incubation time extends to 80 min. Therefore, the optimal acidity, incubation temperature and incubation time for the determination of RA are pH 7, 40 °C and 80 min, respectively. Besides, the effect of different radiation time of the 808 nm laser on the readout of photothermal signal has also been evaluated. Fig. S5d (Supporting information) shows the temperature changes of Y:Yb/Er-Cit-CD, Y:Yb/Er-Cit-CD + oxTMB and Y:Yb/Er-Cit-CD + oxTMB + RA during 10 min irradiation. With the extension of radiation time, Y:Yb/Er-Cit-CD + oxTMB (red curve) and Y:Yb/Er-Cit-CD + oxTMB + RA (green curve) display visible increases followed by gradual stabilization in temperature, but no obvious change is observed in Y:Yb/Er-Cit-CD (black curve). In order to facilitate temperature measurement, 5 min is finally selected as the irradiation time for the subsequent readout of photothermal signal.

Under optimal conditions, we have evaluated the detection potential of the triple-signal sensing system by including various concentrations of RA. The fluorescence emission spectra at different RA concentrations are shown in Fig. 5a. As the concentration of RA increases sequentially, the fluorescence intensity recovers gradually at 550 nm. The inset visually shows the recovery of the fluorescence intensity and is matched to the fluorescence spectrum. More importantly, there is an excellent linear relationship between fluorescence intensity and RA concentration in the range of 0.01–5 μmol/L (Fig. 5b). The fitted regression equation is $F = 337.4X + 1435$ ($R_F^2 = 0.9997$). According to the 3σ rule, the limit of detection (LOD) for fluorescence is 0.004 μmol/L. Next, Fig. 5c displays that as the concentration of RA increases, the absorption at 650 nm gradually decreases due to the reduction of oxTMB to TMB. The inset displays that the blue of the solution slowly fades, which is consistent with the change in the ultraviolet absorption spectra. From Fig. 5d, the well-linear relationship between UV-vis absorbance and RA concentration in the range of 0.1–6 μmol/L can be seen. The corresponding linear regression equation is $A = -0.1309X + 1.150$ ($R_A^2 = 0.9951$), and the LOD for absorption is 0.036 μmol/L. Afterward, the systems containing various levels of RA have been irradiated with 808 nm laser light for 5 min and the temperature changes have been measured by a thermometer.

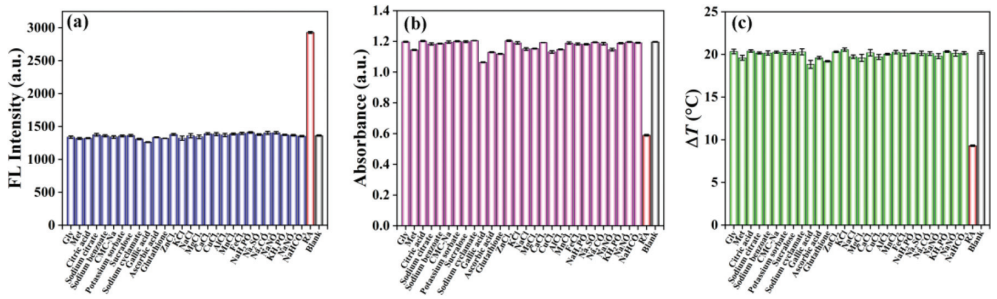

Fig. 6. (a) Fluorescence intensity response, (b) absorbance response and (c) temperature change of Y:Yb/Er-Cit-CD/oxTMB sensing system in the presence of foreign substances.

Table 1
Determination of RA in real sample.

Sample name	HPLC (μmol/L)	Fluorometric			Colorimetric			Photothermic		
		Detection (μmol/L)	Recovery (%)	RSD (%)	Detection (μmol/L)	Recovery (%)	RSD (%)	Detection (μmol/L)	Recovery (%)	RSD (%)
Perilla plum slices	0.7806	0.7369	94.4	0.12	0.8440	108.1	0.13	0.8321	106.6	1.77
Rosemary bread	0.7087	0.6744	95.2	0.23	0.6983	98.5	0.43	0.6890	97.2	2.39
Perilla seed oil	0.2281	0.2209	96.8	0.16	0.2235	98.0	0.47	0.2332	102.3	1.45
Prunella vulgaris granules	1.2773	1.3179	103.2	0.17	1.2973	101.6	0.23	1.3141	102.9	1.15
Perilla drink	0	In Table S2								
Perilla green plum wine	0	In Table S2								

As can be seen in Fig. 5e, the temperature in the system gradually weakens as the amount of RA increases. And in the range of 0.1–6 μmol/L, there is a well-linear correlation between the temperature variation and the amount of RA (Fig. 5f). The related linear equation is $\Delta T = -1.728X + 17.77$ ($R_{\Delta T}{}^2 = 0.9932$), with a LOD of 0.043 μmol/L.

Furthermore, the RA detection performance of this test triple-signal sensor is compared with reported methods, as shown in Table S1 (Supporting information). The comparison shows that the triple-signal sensing system has a lower LOD than most methods, indicating its excellent responsiveness. Significantly, our triple-signal readout analysis method of fluorescence, colorimetric and photothermal not only combines the synergistic benefits of sensitivity, visibility and portability, but the three modes can also be validated against each other to provide more reliable results.

Possible co-existing substances have been analyzed to evaluate the specificity of the Y:Yb/Er-Cit-CD/oxTMB sensing system for the detection of RA. In Fig. 6a, the fluorescence intensity of the solution is significantly enhanced by the introduction of RA, while the change is weak in the presence of interfering substances. Then, Fig. 6b expresses that the variations caused by interfering substances are slight compared to the significant decrease in the absorbance induced by RA. Moreover, from Fig. 6c, it can be seen that the temperature increment of the system drops measurably in the presence of the target RA, but no effect on weakening the temperature increment is observed for other interfering substances. Therefore, these results have demonstrated that the triple-signal sensor has performed excellent selectivity for the determination of RA.

The sensing system has been investigated to detect RA in real samples, and the results are compared with HPLC (Table 1). Except for Perilla drink and Perilla green plum wine where RA is not detected, the levels of RA detected in the real samples ranged from 0.2209 μmol/L to 1.3179 μmol/L. The detection results of Y:Yb/Er-Cit-CD/oxTMB sensing system are consistent with the HPLC results. The test results after adding different concentrations of RA (0.5, 2, 4 μmol/L) to Perilla drink and Perilla green plum wine are shown in Table S2 (Supporting information). The relative standard deviations (RSD) of the test results of all real samples are less than 2.5%, with recoveries in the range of 94.4%−108.1%, indicating the potentiality of the Y:Yb/Er-Cit-CD/oxTMB triple-signal sensing system in the real sample detection.

In general, a new up-conversion fluorescence, colorimetric and photothermal triple-signal sensor has been established for the quantitative detection of RA. Under 980 nm NIR radiation, the Y:Yb/Er-Cit-CD nanoparticles can emit green fluorescence concentrated at 550 nm. The fluorescence emission spectrum overlaps with the UV-vis absorption spectrum of oxTMB, leading to the quenching of the green fluorescence. Then, when the colored oxTMB is reduced to colorless TMB by RA, the fluorescence is restored. Thus, RA can be easily determined by measuring the change in fluorescence signal. At the same time, due to the color difference between oxTMB and TMB, as well as the ability of oxTMB to convert light into heat, the readout of RA with colorimetric and photothermal signals is realized. The experimental results show that the RA concentration has a well-linear relationship with fluorescence, absorbance and temperature change, respectively. In particular, our triple-signal sensor analysis method of fluorescence, colorimetric and photothermal can be mutually tested to improve the reliability of the measurement results in the actual environment. Finally, we have demonstrated the potential application of the system in food samples.

Declaration of competing interest

The authors declare that they have no known competing financial interests or personal relationships that could have appeared to influence the work reported in this paper.

Acknowledgments

This study was supported by the National Natural Science Foundation of China (No. 21305097), General Project of Education Department in Sichuan (No. 035Z2270), Sichuan Key Discipline Construction Project of Traditional Chinese Medicine (No. 2021-16-4) and Double-Support Plan of Disciplinary Construction in Sichuan Agricultural University -Innovation Team Projects (No. P202108).

We would be grateful to Doctor Peng Wu (Analytical&Testing Center, Sichuan University) for his help in testing the fluorescence decay dynamics.

Supplementary materials

Supplementary material associated with this article can be found, in the online version, at doi:10.1016/j.cclet.2022.108099.

References

[1] G.D. Kim, Y.S. Park, Y.H. Jin, C.S. Park, Appl. Microbiol. Biotechnol. 99 (2015) 2083–2092.
[2] M. Alagawany, M.E. Abd El-Hack, M.R. Farag, et al., Anim. Health Res. Rev. 18 (2017) 167–176.
[3] A.G. Adomako-Bonsu, S.L.F. Chan, M. Pratten, J.R. Fry, Toxicol. in Vitro 40 (2017) 248–255.
[4] L.M. Ge, M.J. Zhu, X.Y. Li, et al., Food Hydrocoll. 83 (2018) 308–316.
[5] C.X. Luo, L. Zou, H.J. Sun, et al., Front. Pharmacol. 11 (2020) 153.
[6] F.J. Mirza, S. Amber, Sumera, et al., Phytomedicine 83 (2021) 153490.
[7] Y. Zhang, J.P. Smuts, E. Dodbiba, et al., J. Agric. Food Chem. 60 (2012) 9305–9314.
[8] Y. Liu, X.R. Li, Y.H. Li, et al., J. Pharm. Biomed. Anal. 53 (2010) 698–704.
[9] M. Ozturk, M.E. Duru, B. Ince, et al., Food Chem. 123 (2010) 1352–1356.
[10] S. Baskan, N. Oztekin, F.B. Erim, Food Chem. 101 (2007) 1748–1752.
[11] G. Maduraiveeran, M. Sasidharan, V. Ganesan, Biosens. Bioelectron. 103 (2018) 113–129.
[12] Y.W. Rong, M.M. Hassan, Q. Ouyang, Q.S. Chen, Compr. Rev. Food. Sci. Food Saf. 20 (2021) 3531–3578.
[13] D.M. He, M.M. Yan, P.J. Sun, et al., Chin. Chem. Lett. 32 (2021) 2994–3006.
[14] S.N. Lei, H. Cong, Chin. Chem. Lett. 33 (2022) 1493–1496.
[15] W.T. Li, X.N. Zhang, X.T. Hu, et al., J. Hazard. Mater. 408 (2021) 124872.
[16] L.Z. Liu, Z. Mi, X.Y. Huo, et al., Food Chem. 368 (2022) 130829.
[17] Z.S. Zhang, Y. Gao, P. Li, et al., Chin. Chem. Lett. 31 (2020) 2725–2729.
[18] J.L. Liu, L.L. Lu, A.Q. Li, et al., Biosens. Bioelectron. 68 (2015) 204–209.
[19] H. Yang, X. Chen, J. Wu, et al., Sens. Actuators B: Chem. 290 (2019) 656–665.
[20] Y.Y. Chen, T.T. Zhang, X.N. Gao, et al., Chin. Chem. Lett. 28 (2017) 1983–1986.
[21] Y.C. Chan, C.W. Chen, M.H. Chan, et al., Biosens. Bioelectron. 80 (2016) 131–139.
[22] J.W. Chung, Z. Gerelkhuu, J.H. Oh, Y.I. Lee, Appl. Spectrosc. Rev. 51 (2016) 678–705.
[23] W.T. Xue, Z.H. Di, Y. Zhao, et al., Chin. Chem. Lett. 30 (2019) 899–902.
[24] D. Lu, H. Jiang, G.Y. Zhang, et al., ACS Appl. Mater. Interfaces 13 (2021) 25738–25747.
[25] N.N. Liang, X.T. Hu, W.T. Li, et al., Food Chem. 343 (2021) 128494.
[26] X.M. Li, R.R. Zhao, Y.L. Wei, et al., Chin. Chem. Lett. 27 (2016) 813–816.
[27] L.H. Su, Y.Q. Chen, L.L. Wang, et al., Sens. Actuators B: Chem. 331 (2021) 129431.
[28] H. Wang, X.M. Wu, S.X. Yang, et al., Food Chem. 286 (2019) 322–328.
[29] X.M. Sun, Y. Li, Q. Yang, et al., Chin. Chem. Lett. 32 (2021) 1780–1784.
[30] Y.F. Duan, Q. Li, P.P. He, et al., Chin. Chem. Lett. 33 (2022) 3217–3220.
[31] Y.Y. Zhang, T.F. Zhao, X.H. Zhang, et al., Sens. Actuators B: Chem. 346 (2021) 130494.
[32] D.Y. Yi, Z.X. Wei, W. Zheng, et al., Sens. Actuators B: Chem. 323 (2020) 128691.
[33] L. Miao, Q. Nie, J.L. Wang, et al., Appl. Catal. B 248 (2019) 466–476.
[34] Y. Liu, Q. Ouyang, H.H. Li, et al., ACS Appl. Mater. Interfaces 9 (2017) 18314–18321.
[35] Q. Long, A.J. Fang, Y.Q. Wen, et al., Biosens. Bioelectron. 86 (2016) 109–114.
[36] D.Q. Fan, E.K. Wang, S.J. Dong, Mater. Horiz. 6 (2019) 375–384.
[37] D.Q. Fan, J. Wang, E.K. Wang, S.J. Dong, Chem. Sci. 10 (2019) 7290–7298.